The Astrophysical Journal, 720:1254–1261, 2010 September 10 doi:10.1088/0004-637X/720/2/1254

SPECTROSCOPIC ANALYSIS OF AN EIT WAVE/DIMMING OBSERVED BY *HINODE*/EIS

F. Chen[1,2], M. D. Ding[1,2], and P. F. Chen[1,2]
[1] Department of Astronomy, Nanjing University, Nanjing 210093, China; dmd@nju.edu.cn
[2] Key Laboratory for Modern Astronomy and Astrophysics (Nanjing University), Ministry of Education, Nanjing 210093, China
Received 2009 December 23; accepted 2010 July 5; published 2010 August 19

ABSTRACT

EUV Imaging Telescope (EIT) waves are a wavelike phenomenon propagating outward from the coronal mass ejection source region, with expanding dimmings following behind. We present a spectroscopic study of an EIT wave/dimming event observed by the *Hinode*/Extreme-ultraviolet Imaging Spectrometer. Although the identification of the wave front is somewhat affected by the pre-existing loop structures, the expanding dimming is well defined. We investigate the line intensity, width, and Doppler velocity for four EUV lines. In addition to the significant blueshift implying plasma outflows in the dimming region as revealed in previous studies, we find that the widths of all four spectral lines increase at the outer edge of the dimmings. We illustrate that this feature can be well explained by the field line stretching model, which claims that EIT waves are apparently moving brightenings that are generated by the successive stretching of the closed field lines.

Key words: line: profiles – Sun: corona – Sun: UV radiation – waves

1. INTRODUCTION

EUV Imaging Telescope (EIT) waves were first observed by the EIT aboard the *Solar and Heliospheric Observatory* (*SOHO*; Moses et al. 1997; Thompson et al. 1998). They are best seen in the running difference images as bright fronts with a propagation speed of <500 km s^{-1}, followed by an expanding dimming region (Thompson et al. 1998). More properties of EIT waves were presented by Delannée & Aulanier (1999), Klassen et al. (2000), and Thompson et al. (2009). EIT waves can be observed at several wavelengths, such as 175 Å, 195 Å, 284 Å, and 304 Å (Wills-Davey & Thompson 1999; Zhukov & Auchère 2004; Long et al. 2008). Regarding the relationship between EIT waves and coronal mass ejections (CMEs), Patsourakos & Vourlidas (2009) claim that the EIT wave front is outside the CME frontal loop, whereas Chen (2009) and Dai et al. (2010) claim that the EIT wave front is cospatial with the white-light frontal loop of CMEs.

Moreton waves are another kind of wavelike phenomenon seen in the chromosphere. They are seen as arclike Hα disturbances propagating to a large distance away from the eruption site, with velocities ranging from 500 to 2000 km s^{-1} (Moreton & Ramsey 1960). It was suggested that the footprints of a coronal fast-mode wave or shock wave sweeping the chromosphere, as the wave moves through the tenuous corona, would produce the apparent propagation of Hα disturbances (Uchida 1968). This implies the existence of a fast-mode shock wave in the corona, although it was not observed directly at that time.

After EIT waves were discovered, they were first suggested to be the coronal counterparts of Moreton waves. Therefore, according to Uchida's model, EIT waves were considered to be a fast-mode magnetohydrodynamic (MHD) wave. For example, Wang (2000) found that the ray path of fast-mode waves matches the propagation of the EIT wave fronts, as well as reproducing their tendency of avoiding active regions and coronal holes. Wu et al. (2001) performed a three-dimensional numerical simulation of the perturbation resulting from a pressure pulse. Their result showed that the fast-mode wave front could reproduce many properties of the observed EIT waves. More events were analyzed by Warmuth et al. (2001, 2004), who found that similar propagating features appear in the coronal and chromospheric spectral lines and suggested that they are signatures of the same physical disturbance, i.e., a freely propagating fast-mode MHD shock. However, an obvious problem of the fast-mode wave explanation is that the speeds of EIT waves are statistically >3 times smaller than those of Moreton waves. Wu et al. (2001) and Warmuth et al. (2004) noticed that Moreton waves are visible only near the flare sites, while EIT waves are mostly observed at larger distances. Therefore, they suggested that the speed difference could be a result of deceleration during the wave propagation, which, however, was not supported by Eto et al. (2002). One the other hand, considering the behaviors of EIT waves when they encounter magnetic separatrices, Delannée (2000) suggested that the bright front may be a result of compression of coronal plasma, caused by the interaction between CME-induced expansion of magnetic field lines and surrounding field lines. Chen et al. (2002, 2005) performed numerical simulations of the MHD process of the CME-induced perturbation and found a piston-driven shock running ahead and a slower moving wavelike structure following behind. They proposed that the former corresponds to the coronal Moreton waves while the latter corresponds to the EIT waves. This model was supported by Harra & Sterling (2003), who presented a *TRACE* observation of a fast moving "weak wave" with almost no line-of-sight (LOS) mass motion and a slower moving "bright wave" followed by prominent dimmings.

Spectroscopic observations can provide more insight into the physical nature of EIT waves. Asai et al. (2008) presented a spectroscopic observation of an MHD fast-mode shock wave visible in soft X-rays. Unfortunately, some of the EIT images suffered from scattered light in the telescope; therefore, the EIT wave front was unclear. In this paper, we present a *Hinode*/Extreme-ultraviolet Imaging Spectrometer (EIS) observation of an EIT wave event. We obtain not only the high-resolution Doppler velocity in the region that the wave passes through but also the line width distribution for the first time. We describe the observation and data analysis in Section 2; our results are shown

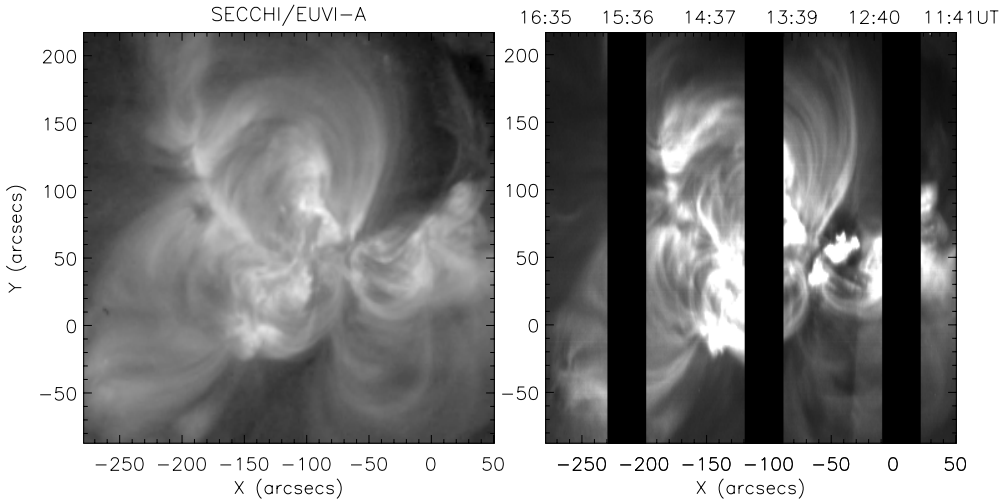

Figure 1. SECCHI/EVUI-A 195 Å image at 12:32:00 UT and EIS Fe XII λ195.12 image from 11:41:23 UT to 16:35:03 UT.

Table 1
EIS Lines Used in This Study

Ion	Wavelength (Å)	log T_{max} (K)
Fe XII....	195.12	6.1
Fe XIII...	202.04	6.2
Fe XIV...	274.20	6.3
Fe XV....	284.16	6.4

in Section 3, followed by discussions about the mechanism of line broadening and its implication to the model of EIT waves in Section 4.

2. OBSERVATIONS AND DATA ANALYSIS

The EIT wave event that we study here occurred in the active region NOAA 10956 on 2007 May 19. It was associated with a B9 flare and a CME. *SOHO*/EIT was in CCD bakeout during the event, while the Extreme UltraViolet Imager (EUVI) on board the *Solar TErrestrial RElations Observatory* (*STEREO*; Howard et al. 2008) observed the event in four wavebands. This event, in particular the propagation speed, has been investigated by Long et al. (2008) and Veronig et al. (2008).

The event was also observed by EIS. The EIS observation of NOAA 10956 started at 11:41:23 UT and ended at 16:35:03 UT using the 1″ slit that rastered across the active region with a step of 1″ and an exposure time of 40 s. The time gap is around 13.5 s between successive exposures. The field of view (FOV) is 330″ in the raster direction and 304″ in the slit direction. The EIS observation covered the EIT wave event. It thus provides a good opportunity to make a spectroscopic study of the EIT wave and the ensuing dimmings.

The details of the EIS instrument are described in Culhane et al. (2007). The two EIS detectors cover the wavelength ranges 170–210 Å and 250–290 Å, therefore providing spectral lines in a wide range of emission temperatures. The EIS has 1″, 2″ slits and 40″, 260″ slots available. The slit raster obtains high spectral resolution data, while the slot observation provides transition region and coronal monochromatic images.

We process the raw data using eis_prep.pro in SSW. This process flags bad data points and converts DN to physical units (erg cm^{-2} s^{-1} sr^{-1} Å^{-1}). For this particular study, we select several coronal lines with a broad range of temperatures, as listed in Table 1. The Fe XIV λ274.20 line is blended with the Si VII λ274.18 line, while this contamination can be estimated by the ratio of the Si VII λ274.18 and λ275.35 lines. In this observation, we find that the intensity of the Si VII λ275.35 line is rather weak, thus the Si VII λ274.18 line is almost mixed with the noise of the background. Therefore, we ignore the blending as Young et al. (2007) suggested. Finally, we make Gaussian fittings to all the lines using mpfitexpr.pro in SSW, with a fitting range of ±0.2 Å from the default line center.

To study the wave phenomena, we should co-align the EIS observation with the *STEREO-A*/EUVI observation. We calculate the correlation between the Fe XII 195 Å image from EUVI-A at 12:32 UT and the intensity map obtained from EIS for the same emission line, using a 50″×50″ box in order to get the offsets. Figure 1 shows the EUVI and EIS data after co-alignment, where their correlation coefficient is as high as ∼95%. Since *STEREO A* and *Hinode*/EIS view the Sun from different angles, the co-alignment of optical-thin EUV images should take the stratified structure into account, which involves the tomography technique using both *STEREO A* and *B* images. Fortunately, *STEREO A* and *Hinode* were separated by only ∼4° on 2007 May 19, which makes the direct translation sufficient as indicated by the high correlation coefficient.

For this event, Long et al. (2008) found that the EIT wave front propagated at a low velocity initially and significantly accelerated at around 12:50 UT in high-cadence SECCHI/EUVI-A 171 Å data (see the left column of Figure 3 in their paper). Figure 2 shows the relation between the EIS scan and the EIT wave seen from the base difference images of SECCHI-A 171 Å and 195 Å. The arc-like brightening was first seen at 12:41 UT in the 171 Å image and at 12:42 UT in the 195 Å image, while it was most clearly identified after 12:51 UT. Unfortunately, the leading edge of the wave front was out of the EIS FOV at that time, with only part of the brightening still lying in the EIS FOV. The whole wave front propagated out of the EIS FOV after 12:54 UT. The EIS raw data recorded the observation time of all rasters; therefore, we can identify the time and position of the rasters when they encountered the EIT wave. We find that the slit positions from $x \sim -21''$ to $x \sim -27''$ and those from $x \sim -28''$ to $x \sim -34''$ correspond to the initial and acceleration stages of the EIT wave, respectively. It is possible that some of the brightening seen near the active region during the early time may be due to the displacement of pre-existing loop

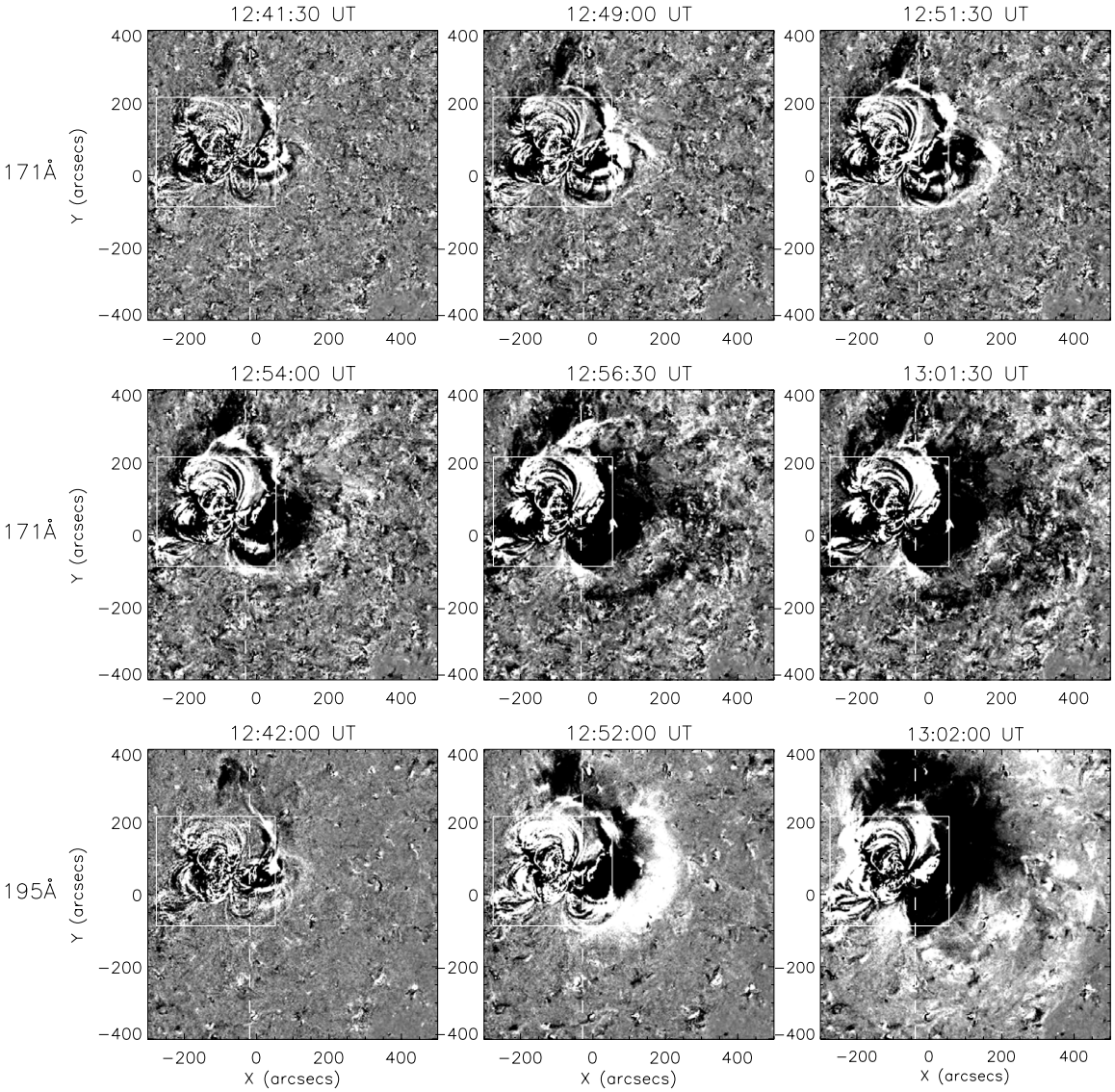

Figure 2. Base difference images of SECCHI/EUVI-A 171 Å (top and middle rows) and 195 Å (bottom row). The images at 171 Å are subtracted by the image at 12:31 UT and the images at 195 Å are subtracted by the image at 12:32 UT, with the solar rotation corrected. The white boxes indicate the FOV of EIS. The dashed vertical lines represent the position of the silt at the time of each panel.

structures. In fact, at least to some extent, the coronal loops can affect the identification of the wave front and the measurement of its width.

3. RESULTS

After processing the co-aligned data sets, we analyze the EIT wave on 2007 May 19 in detail using the EIS observations. We obtain the line intensity, line width, and Doppler velocity for several lines with different formation temperatures. Figure 3 shows the line intensity, line width, and Doppler velocity for the Fe XII λ195.12, Fe XIII λ202.04, and Fe XV λ284.16 lines. Figure 4 presents the results of the region of interest (a zoomed view of the white box in Figure 3). We also analyze the EIS observation of the same active region at about 3 hr before the eruption, with the results shown in Figure 5.

We measure the positions of the wave front from 12:42 to 12:52 UT using the 195 Å data and those from 12:46 to 12:54 UT using the 171 Å data. The vertical bars in Figure 4 indicate the width of the bright structure and its propagation during a single EIS exposure; the horizontal ones indicate the accuracy of EIS–EUVI co-alignment, i.e., $\sim 2''$. Note that the red bar at 12:54 UT is completely out of the EIS FOV.

3.1. The Intensity Decrease

We compose the two-dimensional images for the 3 EUV lines from each scan in the left column of Figure 3, although the emissions are not simultaneous in the E–W direction. Note that we have adjusted the color scale to illustrate more clearly the intensity variation so that the core of the active region is saturated. In contrast to the *STEREO*/EUVI-A image (shown in Figure 1, left panel), the intensity in the region to the east of $x \sim -30''$ is significantly lower than that in the region to the west. The boundary of intensity decrease is inclined to the slit direction by a small angle, because the slit was moving along the W–E direction while the dimming region expanded southward. Furthermore, it is just to the left of (i.e., behind) the red dotted line, an indicator of the wave front propagation, as shown in Figure 4. Therefore, this region of intensity decrease in the EIS map is considered to be the dimming region associated with the EIT wave. The left panel of Figure 5 shows that there is

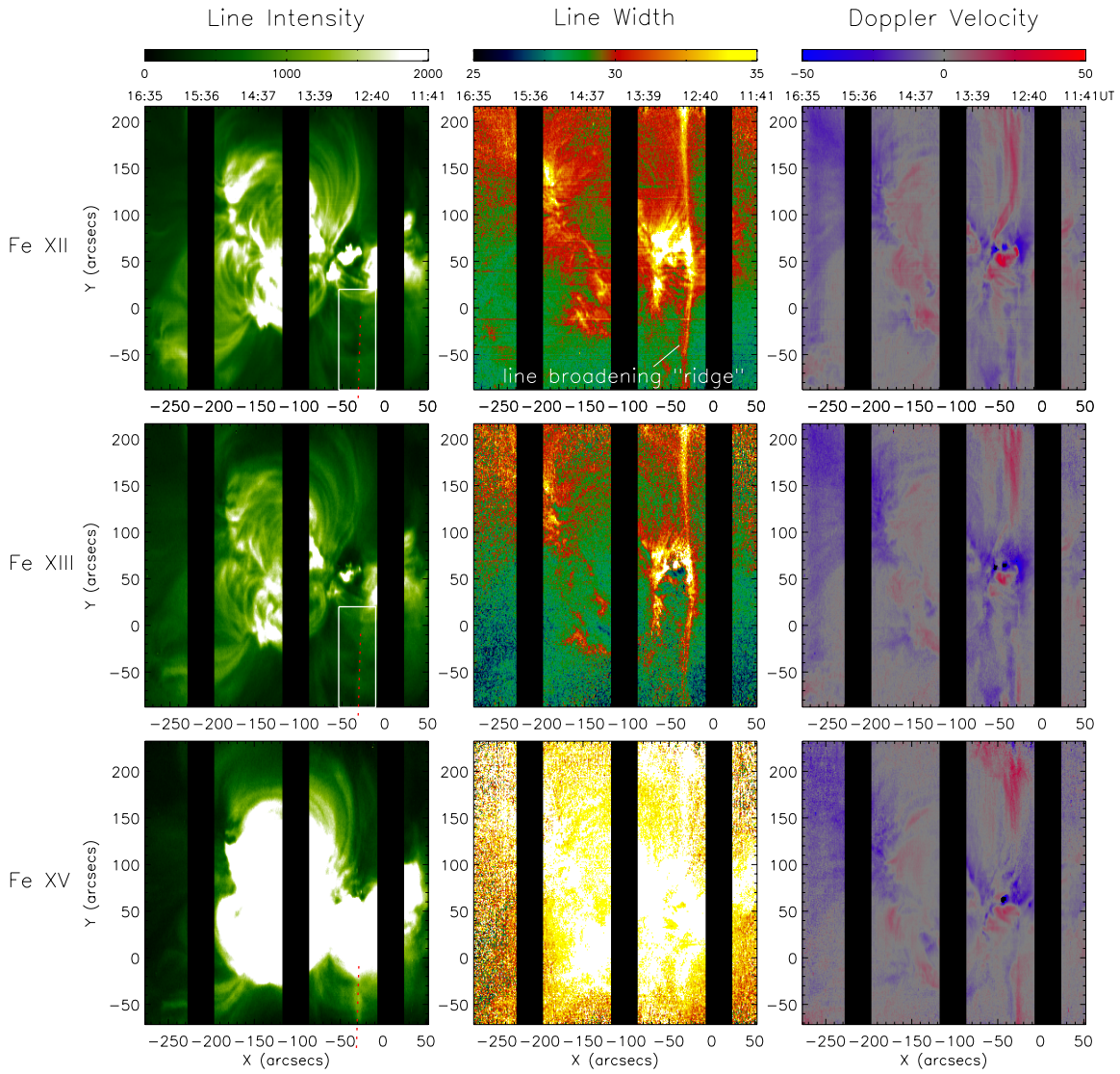

Figure 3. Line intensity (left), width (middle), and Doppler velocity (right) from 11:41:23 UT to 16:35:03 UT for three coronal lines. From top to bottom, the three rows are the Fe XII λ195.12, Fe XIII λ202.04, and Fe XV λ284.16 lines, respectively. The red dotted line is the same as that in Figure 4. The white boxes indicate the region which is studied in detail below. Note that the FOV of the Fe XV image is actually different from that of the Fe XII and Fe XIII images, because of the offset between the two CCDs of EIS.

no intensity decrease near $x \sim -30''$; therefore, the intensity decrease during the eruption should not be a feature of the active region itself, such as a coronal hole.

By investigating the intensity maps of different lines, we find that the intensity decrease is prominent in the Fe XII and Fe XIII lines, while it is not evident in the Fe XIV and Fe XV lines as well as the transition region lines like He II λ256.32. From Figure 4, one can find a brightening feature just along the red dashed line in Fe XIII. It is supposed to be the bright wave front. The low contrast of the brightening feature reflects a systematic drawback of observing fast propagating structures using a long exposure time and a low raster cadence of the EIS. The propagation distance of the wave front during a single EIS exposure, which is at least 10″ (depending on the wave propagation speed), is roughly comparable with the width of the wave front seen in the 171 Å images. This makes the wave front look very fuzzy in the figure reconstructed from the scanning observation. For this event, the wave front is also seen in the 284 Å image of EUVI, which is wider than that seen in the 171 and 195 Å images, especially in the southern part (Figure 1 in Long et al. 2008). By comparison, the wave front seen in the image of the Fe XV line of EIS is the clearest. Furthermore, we find that the image contrast of EIS, defined as the ratio of the maximum value of the active region to the average value over a quiescent region, is lower than that of EUVI, since the quiescent value of the EIS image is much higher than that of the EUVI, while the maximum values are not significantly different. This can explain the lower contrast of the wave front seen in the EIS images compared to that in the EUVI images.

We calculate the average intensity on both sides of the dimming boundary. The bottom 70 rows are selected and divided into three parts along the slit direction. The areas selected are marked by dashed, dotted, and solid boxes in the first and fourth panels in Figure 4. The result is shown in Figure 6, using the same line styles as in Figure 4. The intensity in the dimming region is 23% and 21% less than that in the pre-wave region for the Fe XII and Fe XIII lines, respectively. Furthermore, the intensity in the wave front region is 11% higher than that in

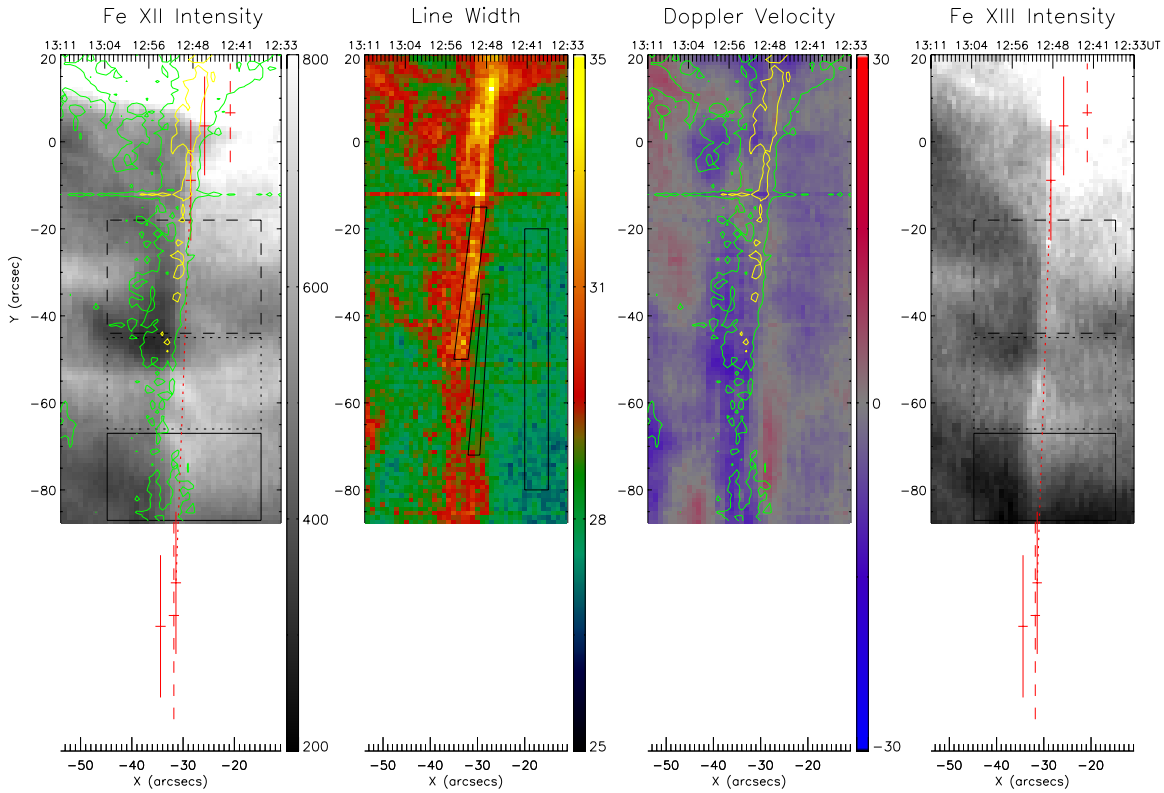

Figure 4. Zoomed view of the line broadening "ridge," an enlargement of the white box shown in Figure 3. The left three panels show the line intensity, width, and Doppler velocity for the Fe XII λ195 line and the right panel shows the intensity for the Fe XIII λ202.04 line. The red solid and dashed vertical bars in the first and fourth panels indicate the wave front measured from the EUVI-A 171 and 195 Å images, respectively. The middle points of the bars at 12:49 and 12:51 UT measured from the 171 Å image are connected by the red dotted line that corresponds to the wave front *propagation* during the observation gap. The intensity and LOS velocity for the Fe XII line are overlaid by the contours of the line width, with contour levels of 30 mÅ (green) and 32 mÅ (yellow). The rectangles in the first and fourth panels indicate the area selected for calculation of the intensity decrease. The dashed, dotted, and solid lines are for Y positions of $-18''$ to $-44''$, $-45''$ to $-66''$ and $-67''$ to $-87''$, respectively. The quadrilaterals in the second panel indicate the areas selected for calculation of the line width.

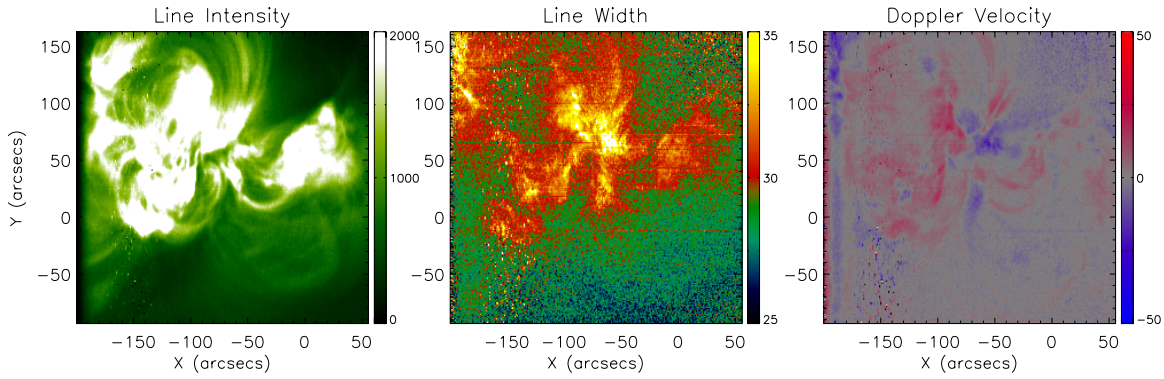

Figure 5. Line intensity, width, and Doppler velocity maps for the Fe XII λ195.12 line for the active region before the eruption. The scanning time is from 09:42:12 UT to 10:31:24 UT. There is no significant structure in the southern part of the active region, in particular in the width and velocity maps.

the pre-wave region for the Fe XIII line. This calculation for the wave front is not applied to the Fe XII line, since the wave front is not clear enough for this line.

3.2. The Doppler Velocity

In order to study the LOS velocity, the EIS slit tilt and the *Hinode* orbital variation effects must be corrected. We use spline fitting to correct the orbital variation. Note that those data points that are during or close to the eclipse periods (i.e., columns 50–80, 160–190, and 270–300 in the data array) are ignored by manually setting their weights to be zero. Since the active region is close to the solar disk center, the projection effect is negligible.

The results show that there is a blueshift of more than 10 km s^{-1} appearing in the dimming region. Note that an uncertainty may exist in the Doppler velocity due to the processing of the orbit variation, which is much smaller than the blueshift. Additionally, similar to what we have discussed above, before the eruption there is little mass motion in the region where the dimmings are later observed (see Figure 5, right panel). Therefore, the existence of the outflows in the dimming region is of physical significance. In some previous investigations on EIT wave or eruption events, e.g., Harra & Sterling (2003) and Asai

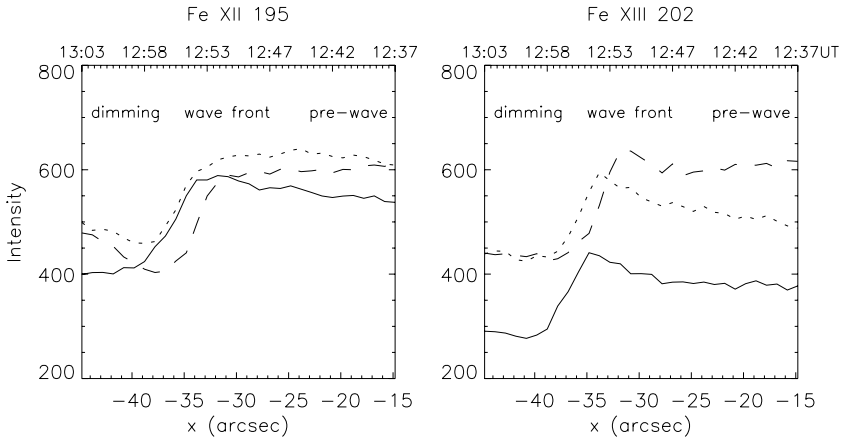

Figure 6. Average intensity over the *Y*-direction for the three areas indicated in Figure 4 (first and fourth panels), showing the intensity variation across the border of the dimming and the wave front. The line styles are the same as those in Figure 4. The dashed line corresponds to the area close to the source region of the eruption, the dotted line corresponds to an area in the middle, and the solid line corresponds to an area further away. The local intensity minimum for the three lines moves to the left sequentially, implying the propagation of the intersection between the expanding dimming and the slit. In comparison, the wave front for the Fe XII line is not as evident as that for the Fe XIII line.

et al. (2008), line splitting was observed in some coronal lines. These authors performed a two-component Gaussian fitting and obtained a strong blueshift of over 100 km s^{-1} for the moving component. For this event, we search the line profiles at different positions and find no visible line splitting except in a small region around the active region core. Thus, we only make the single Gaussian fitting, which yields outflow velocities much smaller than those in Harra & Sterling (2003) and Asai et al. (2008). Therefore, the velocity values obtained by these two methods cannot be compared quantitatively.

Furthermore, we carefully investigate the spatial distribution of the blueshift in Figure 4. We find that the outflows are generally confined in the dimming region and therefore are behind the EIT wave front, as shown in the first and third panels of Figure 4. It is noted, however, that a patch of blueshifted pattern, which is located around $y \sim -82'' \pm 4''$ and $x \sim -31''$, falls in the region with density enhancement. We also find that, different from the line intensity, the blueshift areas for the Fe XIV and Fe XV lines are similar to those for the Fe XII and Fe XIII lines.

3.3. The Line Broadening

Excess of line width over its thermal broadening is thought to be caused by turbulent mass motions or waves. As shown in the middle column of Figure 3, the line width significantly increases along the boundary of the dimming region, seen as a ridge-like structure. Comparing the result with that shown in Figure 5, it is confirmed that the extra line broadening does not correspond to the active region structures.

The width of the Fe XII λ195.12 line in the background region is about 28 mÅ, while the line width in the "ridge" is generally larger than 30 mÅ. To obtain a more accurate result, we select several points in the "ridge," the wave front, and the pre-wave quiet region, as indicated by the quadrilaterals in the second panel of Figure 4. Note that the position of the middle box in this panel corresponds to the linear interpolation between the wave fronts at 12:49:00 and 12:51:30 UT. The result shows that the average line width in the "ridge" is 31.3 ± 0.9 mÅ, which is 12% broader than that in the quiet region, i.e., 28.0 ± 0.6 mÅ. However, the widths for most of the points selected in the wave front region, i.e., 28.9 ± 0.5 mÅ, are almost the same as those in the quiet region. The nonthermal velocities, $V_{\rm non}$, for the Fe XII line, the observed FWHM for the same line, FWHM$_{\rm obs}$, and the instrumental FWHM, FWHM$_{\rm ins}$, are related by

$$\mathrm{FWHM}_{\rm obs}^2 = \mathrm{FWHM}_{\rm ins}^2 + 4\ln 2 \frac{\lambda^2}{c^2}\left(\frac{2kT}{M} + V_{\rm non}^2\right), \quad (1)$$

where the value of FWHM$_{\rm ins}$ is 0.056 Å, λ is the wavelength (in Å), c is the speed of light, k is the Boltzmann constant, T is the electron temperature, and M is the ion mass. The value of FWHM$_{\rm obs}$ (in Å) can be obtained from Gaussian fitting parameter. The nonthermal velocities, converted from the line widths of the "ridge," the wave front, and the quiet region that are indicated in the second panel of Figure 4, are 39.4 ± 3.4 km s^{-1}, 29.5 ± 2.3 km s^{-1}, and 25.1 ± 3.2 km s^{-1}, respectively.

Furthermore, we investigate the spatial relationship between the line broadening "ridge" and the dimming region in Figure 4. It is found that the location of the "ridge" is generally cospatial with the outer boundary of the dimming region. This may suggest that the EIT wave-induced excess line broadening is most significant at the edge of the dimming region, while it is generally negligible at the EIT wave front. However, it is noticed that a patch of line broadening pattern, which is located around $y \sim -82'' \pm 4''$ and $x \sim -31''$, falls in the region with density enhancement. This line broadening patch also presents blueshift as illustrated in Section 3.2. This seems to give us an impression that some part of the EIT wave front may also present strong outflows and line broadenings. After examining carefully the EUVI 195 Å images in Figure 2 (the bottom row, mainly the middle panel), we find that the density enhancement comes from some bright loops embedded in the dimming region, rather than the EIT wave front. This implies that the EIT wave front propagation, as denoted by the red dotted line in the first panel of Figure 4, does not follow a strictly straight line and may turn out to be more vertical from $(x, y) \sim (-30'', -50'')$. Note that a more vertical line in the left panel of Figure 4 means a larger propagation velocity. We also note that the width of the Fe XIII λ202.04 line shows a similar distribution to that of the Fe XII λ195.12 line, while the "ridge" is not significant in the Fe XIV and Fe XV lines.

4. DISCUSSION

EIT waves and the ensuing expanding dimmings are intriguing phenomena. It was suggested that both of them result from

the same process (Chen et al. 2005). However, the nature of EIT waves is still under hot debate. While many researchers consider EIT waves to be fast-mode MHD waves (Pomoell et al. 2008; Patsourakos & Vourlidas 2009; Kienreich et al. 2009; Gopalswamy et al. 2009), others believe that they are non-wave perturbations (Delannée 2000; Chen et al. 2002; Attrill et al. 2007; Delannée et al. 2008; Zhukov et al. 2009). Spectroscopic observations can help clarify the nature of EIT waves.

Harra & Sterling (2001) discovered that there is a strong outflow in the dimming through spectroscopic observations. Later, they found that there is nearly no Doppler velocity at the EIT wave front (Harra & Sterling 2003). In this paper, we analyze the *Hinode*/EIS observations of an EIT wave/dimming event. The results confirm the Doppler velocity distribution found by Harra & Sterling (2001, 2003). These results are consistent with the model of Chen et al. (2002), which simultaneously interprets the formation of EIT wave fronts and dimmings in terms of the stretching of magnetic field lines, i.e., field lines are successively stretched to compress plasma at the outer boundary to form bright fronts, with the bulging wake forming the dimmings. We note that the absence of Doppler velocity at the wave front is also compatible with the fast-mode wave interpretation, since the velocity disturbance induced by the wave front would be directed across the LOS in events observed near the disk center.

We also analyze the spectral line widths and find that they may significantly increase at the outer edge of the dimming region. The enhanced line widths associated with outflows were reported both in the active region boundaries (Doschek et al. 2008) and CME-associated dimming regions (McIntosh 2009). Doschek et al. (2008) explained the line broadening as caused by multiplicity of flows, whereas McIntosh (2009) proposed an alternative model in which the broadening may be attributed to the growth of Alfvén wave amplitudes in the rarified dimming region. It requires convective buffeting from the subsurface of the Sun to test the Alfvén wave hypothesis in the MHD modeling of CMEs. Instead, it is practical and interesting to check whether the MHD numerical model of Chen et al. (2002, 2005) can explain the spatial distribution of the EUV line broadening in terms of multiplicity of flows as proposed by Doschek et al. (2008).

We analyze the value at $y = 4.5$ in the simulation result of Chen et al. (2002, 2005). The temperature is approximately the quantity $T_{\max}$ of the Fe XII λ195 line as shown in Table 1 at this height. We define those pixels with 0.8 times the pre-wave density or less as the dimming region and pixels with density greater than the pre-wave value as the wave front. The boundaries of the dimming and the wave front are indicated by the vertical dotted lines in Figure 7. Note that, numerically, there is a smooth transition between them. The top panel of Figure 7 shows the horizontal distributions of plasma density and LOS velocity in the simulation results of Chen et al. (2002, 2005), which are consistent with our observations and those of Harra & Sterling (2001, 2003). In order to derive the spectral line width distribution, we descretize the space in the simulation into pixels according to the *Hinode*/EIS spatial resolution. We then use the difference of the maximum and minimum values of the LOS velocities in each "pixel" to represent the physical effect that would lead to the line broadening. As indicated by the bottom panel of Figure 7, the result shows that the velocity dispersion within each pixel reaches its maximum at the edge of the dimming region but becomes negligible at the wave front. This implies that the field line stretching model of Chen et al. (2002, 2005), which simultaneously accounts for the formation of EIT waves and dimmings, can well explain the observed distribution of line broadening in the dimming regions.

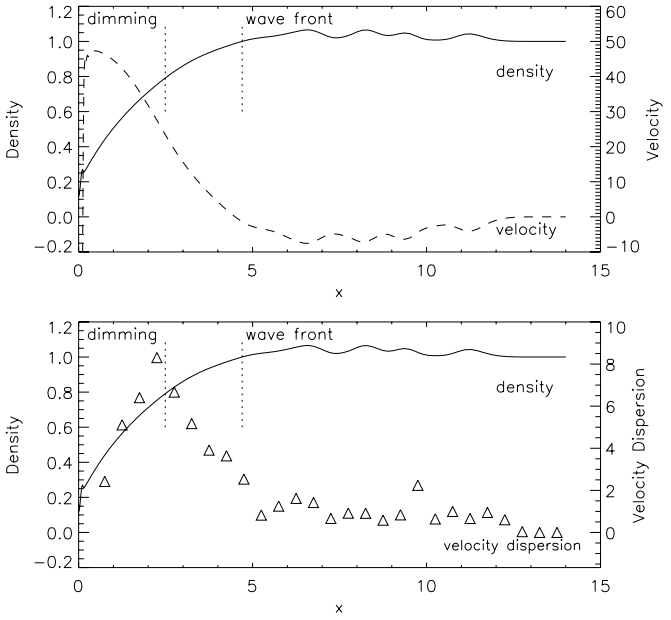

Figure 7. Horizontal distribution of the density, LOS velocity, and velocity dispersion within each pixel at $y = 4.5$ from a snapshot of the numerical model of Chen et al. (2002, 2005). The vertical dotted lines indicate the boundaries of the dimming region and the wave front, as defined in the text. All the physical units are arbitrary. See the text for details.

We thank the referee for constructive comments that helped to improve this manuscript. The research was supported by NSFC under grants 10828306 and 10933003 and by NKBRSF under grant 2006CB806302. *Hinode* is a Japanese mission developed and launched by ISAS/JAXA, collaborating with NAOJ as a domestic partner and NASA and STFC (UK) as international partners. Scientific operation of the *Hinode* mission is conducted by the *Hinode* science team organized at ISAS/JAXA. This team mainly consists of scientists from institutes in the partner countries. Support for the post-launch operation is provided by JAXA and NAOJ (Japan), STFC (UK), NASA, ESA, and NSC (Norway). The SECCHI data used here were produced by an international consortium of USA, UK, Germany, Belgium, and France. We thank the *STEREO*/SECCHI consortium for providing open access to their data.

REFERENCES

Asai, A., Hara, H., Watanabe, T., Imada, S., Sakao, T., Narukage, N., Culhane, J. L., & Doschek, G. A. 2008, ApJ, 685, 622A
Attrill, G. D. R., Harra, L. K., van Driel-Gesztelyi, L., & Démoulin, P. 2007, ApJ, 656, L101
Chen, P. F. 2009, ApJ, 698, L112
Chen, P. F., Fang, C., & Shibata, K. 2005, ApJ, 622, 1202
Chen, P. F., Wu, S.T., Shibata, K., & Fang, C. 2002, ApJ, 572, L99
Culhane, J. L., et al. 2007, Sol. Phys., 243, 19
Dai, Y., Auchère, F., Vial, J.-C., Tang, Y. H., & Zong, W. G. 2010, ApJ, 708, 913
Delannée, C. 2000, ApJ, 545, 512
Delannée, C., & Aulanier, G. 1999, Sol. Phys., 190, 107
Delannée, C., Török, T., Aulanier, G., & Hochedez, J.-F. 2008, Sol. Phys., 247, 123
Doschek, G. A., Warren, H. P., Mariska, J. T., Muglach, K., Culhane, J. L., Hara, H., & Watanabe, T. 2008, ApJ, 686, 1362
Eto, S., et al. 2002, PASJ, 54, 481E
Gopalswamy, N., et al. 2009, ApJ, 691, L123

Harra, L. K., & Sterling, A. C. 2001, ApJ, 561, L215
Harra, L. K., & Sterling, A. C. 2003, ApJ, 587, 429
Howard, R. A., et al. 2008, Space Sci. Rev., 136, 67
Kienreich, I. W., Temmer, M., & Veronig, A. M. 2009, ApJ, 703, L118
Klassen, A., Ausrass, H., Mann, G., & Tompson, B.J. 2000, A&AS, 141, 357
Long, D. M., Gallagher, P. T., McAteer, R. T. J., & Bloomfield, D. S. 2008, ApJ, 680, L81
McIntosh, S. W. 2009, ApJ, 693, 1306
Moreton, G. E., & Ramsey, H. E. 1960, PASP, 72, 357
Moses, D., et al. 1997, Sol. Phys., 175, 571M
Patsourakos, S., & Vourlidas, A. 2009, ApJ, 700, L182
Pomoell, J., Vainio, R., & Kssmann, R. 2008, Sol. Phys., 253, 249
Thompson, B. J., & Meyer, D.C. 2009, ApJS, 183, 225T
Thompson, B. J., Plunkett, S. P., Gurman, J. B., Newmark, J. S., St. Cyr, O. C., & Michels, D. J. 1998, Geophys. Res. Lett., 25, 2465
Uchida, Y. 1968, Sol. Phys., 4, 30
Veronig, A. M., Temmer, M., & Vršnak, B. 2008, ApJ, 681, 113
Wang, Y.-M. 2000, ApJ, 543, L89
Warmuth, A., Vršnak, B., Aurass, H., & Hanslmeier, A. 2001, ApJ, 560, L105
Warmuth, A., Vršnak, B., Magdaleni, J., Hanslmeier, A., & Otruba, W. 2004, A&A, 418, 1117
Wills-Davey, M. J., & Thompson, B. J. 1999, Sol. Phys., 190, 467
Wu, S. T., Zheng, H., Wang, S., Thompson, B. J., Plunkett, S. P., Zhao, X. P., & Dryer, M. 2001, J. Geophys. Res., 106, 25089
Young, P. R., et al. 2007, PASJ, 59, S857
Zhukov, A. N., & Auchère, F. 2004, A&A, 427, 705
Zhukov, A. N., Rodriguez, L., & de Patoul, J. 2009, Sol. Phys., 259, 73